Cardiovascular Engineering and Technology (2024) 15:383–393
https://doi.org/10.1007/s13239-024-00715-4

BMES BIOMEDICAL ENGINEERING SOCIETY

ORIGINAL ARTICLE

Segmentation and Volumetric Analysis of Heart from Cardiac CT Images

Rashmitha[1] · K. N. Manjunath[1] · Anjali Kulkarni[2] · Vamshikrishna Kulkarni[3]

Received: 7 July 2023 / Accepted: 2 January 2024 / Published online: 30 April 2024

Abstract

Purpose Cardiac CT is a valuable diagnostic tool in evaluating cardiovascular diseases. Accurate segmentation of the heart and its structures from cardiac CT and MRI images is essential for diagnosing functional abnormalities, treatment plans and cardiovascular diseases management. Accurate segmentation and quantitative assessments are still a challenge. Manual delineation of the heart from the scan images is labour-intensive, time-consuming, and error prone as it depends on the radiologist's experience. Thus, automated techniques are highly desirable as they can significantly improve the efficiency and accuracy of image analysis.

Method This work addresses the above problems. A new, image-driven, fast, and fully automatic segmentation method was developed to segment the heart from CT images using a processing pipeline of adaptive median filter, multi-level thresholding, active contours, mathematical morphology, and the knowledge of human anatomy to delineate the regions of interest.

Results The algorithm proposed is simple to implement and validate and requires no human intervention. The method is tested on the 'Image CHD' DICOM images (multi-centre, clinically approved single-phase de-identified images), and the results obtained were validated against the ground truths provided with the dataset. The results show an average Dice score, Jaccard score, and Hausdorff distance of *0.866, 0.776*, and *33.29 mm*, respectively, for the segmentation of the heart's chambers, aorta, and blood vessels. The results and the ground truths were compared using Bland-Altmon plots.

Conclusion The heart was correctly segmented from the CT images using the proposed method. Further this segmentation technique can be used to develop AI based solutions for segmentation.

Keywords Heart chambers · Active contours · Masks · Cardiac CT · Subjective evaluation

Introduction

Cardiovascular diseases (CVD) such as coronary artery disease, heart failure, hypertension, stroke, and arrhythmias are among the leading cause of death in individuals [1]. A WHO factsheet of 2021 states that CVDs account for nearly 32% of all deaths [2]. While genetic conditions may not be treated completely, detecting these diseases at the early stages allows for effective management and treatment. An insight into the internal structures is necessary to treat and diagnose CVD. Cardiac Computed Tomography (CT) Cardiovascular Magnetic Resonance Imaging (MRI) [3] and the coronary angiography are widely employed imaging modalities for structural and functions assessment of the heart respectively. These modalities produce unprecedented high-resolution images of the heart and have become a valuable method for non-invasive evaluation of the heart. These images contain regions of interest (ROI), i.e., heart and blood vessels, along with organs in the vicinity like lungs, ribs, spine, and liver. Image segmentation and extracting the volume of interest (VOI) and shape of the anatomical structures are among the key procedures employed while treating CVD. Separating the heart and its vessels from the rest is essential for further

Associate Editor Derek J. Dosdall, Ph.D. oversaw the review of this article.

✉ K. N. Manjunath
knm_mit@yahoo.com

[1] Department of Computer Science and Engineering, Manipal Institute of Technology, Manipal Academy of Higher Education, Manipal, Karnataka 576104, India

[2] Consultant in Radiation Oncology, Clinical Informatics and Artificial Intelligence, Karkinos Healthcare, Bengaluru, India

[3] Healthcare IT, Softrams, 205 161 Fort Evans Rd, Leesburg, VA 20176, USA

analysis and diagnosis. It enables the computation of cardiac functional parameters like stroke volume, ejection fraction, etc., which are important in assessing cardiac function, heart failure, and congenital heart disease. Manually delineating the ROI is time-consuming, demands technical and clinical knowledge, subject to inter and intra-observer errors, and not easily reproducible. Thus, it is desirable to have automatic segmentation to ensure unbiased, reproducible, and consistent results. Fully automatic whole-heart segmentation has excellent potential for many cardiac applications [4, 5].

For review of state-of-the art techniques, the clinical and technical journals were considered from MEDLINE, PUBMED and Mesh headings databases. Traditionally, segmentation in medical images was performed by a radiologist slice by slice who manually delineates the ROI. This process is time-consuming, error-prone, subject to inter and intra-observer variability, and not reproducible [6]. The accuracy and efficiency of segmentation are paramount since they can affect the clinical decisions. One area of research focuses on hybrid methods for segmentation [4]. These methods involve the use of manual and automated methods. It leverages human interaction and expertise to provide the seed points or initial guidance. These hybrid methods have shown to improve the accuracy and efficiency in segmentation. Model fitting segmentation methods use knowledge of shape and geometry of the ROI [7]. A model is created using training images to learn the characteristics and geometry of the ROI. This model is then applied to new images where it selects the object that matches itself closely. This method is seen to provide robust results and can cope well with deformation in images [8]. There is also research in developing methods using traditional image processing techniques. These are data-driven and considered low-level segmentation algorithms. Studies have used edge detection, region growing, and thresholding techniques to segment the heart. These research efforts indicate the potential of traditional image processing techniques in achieving accurate heart segmentation. Much research has been done on the heart segmentation, but, most of these focus on segmenting just the left ventricle or myocardium, as the quantitative assessment of the left ventricle and myocardium is sufficient for diagnosing many coronary heart diseases [9].

With the rising cases of CVDs, having a fast, consistent, automated, and accurate form of segmentation becomes important. This work aim to devise a fully automatic heart segmentation from the cardiac CT images with the help of image processing techniques and exploiting the human anatomy. It also complements segmentation with a method to calculate the volumes of the extracted ROI to help for faster diagnosis. Hence the aim is defined through two objectives.

- Develop an automated method for segmenting the heart chambers and blood vessels from CT images.
- Compute the volumes and evaluate the accuracy of the method by comparing with the ground truths (GT).

Materials and Methods

The required Cardiac CT images in NifTII format were downloaded from ImageCHD [10] database which has sixteen types of congenital heart diseases. These images were single energy and single-phase CT acquisition. Table 1 details the image acquisition parameters. These images are captured using a SIEMENS biograph^{TM} 64 CT scanner. The image resolution was 512*512*(137–551) with a voxel size of 0.25*0.25*0.5 mm^3. For data privacy, patient demography, image scanner details and clinical details were removed from the nifTII file headers. After image collection, we checked the data completeness (for missing DICOM attributes) and any cases with incomplete tag details were discarded. Certain dataset needed data pre-processing to improve the tissue contrast by reducing the quantum noise. As the quality of the image directly affects the accuracy and efficiency of the segmentation, we considered only diagnostic quality images. The dataset also includes manually delineated GT defined by experts for the whole heart segmentation. The segmentation labels were fulfilled by one radiologist, and seven substructures were labelled: LV, RV, LA, RA, Myocardium, Aorta, and Pulmonary Artery. The manual delineation (GT) was performed by 4 senior cardiologists (32-, 20-, 16-, and 14-years experiences) using MImics software. One cardiologist labelled the segmentation and other three reviewed it. To avoid bias or inter-observer variance among three opinions, the voting policy was followed. Like this, each one worked independently on 25% of the dataset in their image pool and created the GT labels. The results in this work are validated with these labels. We also have included five retrospective cases from Radiodiagnosis and imaging department, Kasturba Hospital, Manipal and there is no plans for prospective cases.

The block diagram of the work is shown in Fig. 1. The segmentation algorithm consists of three major steps. The

Table 1 The Cardiac CT imaging acquisition details

Format	DICOM, nii (nifti)
Patient demography	Anonymized (de-identified according to EDPR)
Source	Multi centre, clinically approved
Sample size	90
Data authenticity	Validated as per DICOM PS3.1 2022b
Dimension	2D, 3D, 4D
Scan date	Last 5-6 years
MDCT	64 and 128 slices
Slice thickness	0.4–1.0 mm

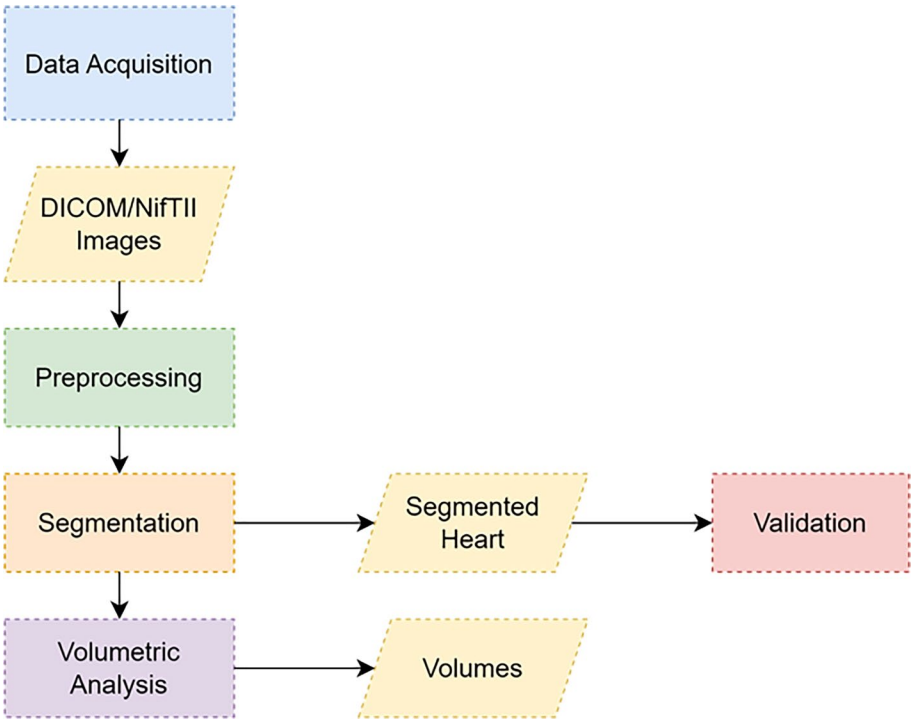

Fig. 1 Methodology of the proposed work

first is the pre-processing of the images for contrast enhancement, calculation of statistical parameters, and removal of noise and extra artifacts. The next step is the segmentation of the heart. The knowledge of human anatomy and the intensity levels corresponding to various organs are used extensively in this step. Each of these steps is explained in detail below.

Pre-processing

Pre-processing is not a mandatory step in medical image processing. It is done based on the clinical task. At the start, the background air, and artifacts like the scanning table (Fig. 2) were removed. The borders and intensity differences between the tissues are also not very prominent. This was resolved to enhance the image quality through following steps.

- Rotate the images to have the spine face downwards to allow for more effortless exploitation of human anatomy during segmentation.
- Contrast enhancement to enhance the intensity differences.
- The quantum noise was reduced using adaptive median filter.
- Computation of statistical parameters to be used during the segmentation stage.

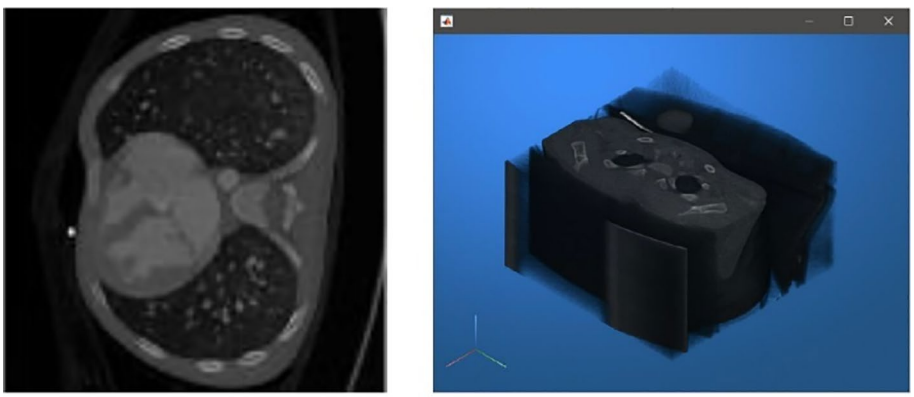

(a) (b)

Fig. 2 Dataset slice and volume **a** Sample slice from the CT image dataset, **b** volume rendering of CT images

- Retain only the largest connected component in the volume to remove all unwanted objects (artifacts).

Statistical Parameters Calculation

In second step, the statistical parameters were calculated for separating the other organs from CT images [11]. Let n, m, and p be the dimensions of the 3D CT scan. Let the CT volume be represented as $f(x, y, z)$, where $x = 1 : n, y = 1 : m, andz = 1 : p$. For each axial slice, the following parameters are computed (Fig. 3):

- **Mean of the pixels, $\mu(k)$:** The image histogram shows several distinct peaks. Of these, the valley points belong to the air, and the highest belongs to bones. The mean μ of the intensities corresponds to the air due to its predominance and can be used to separate the air and background from the rest of the image (Fig. 4b).

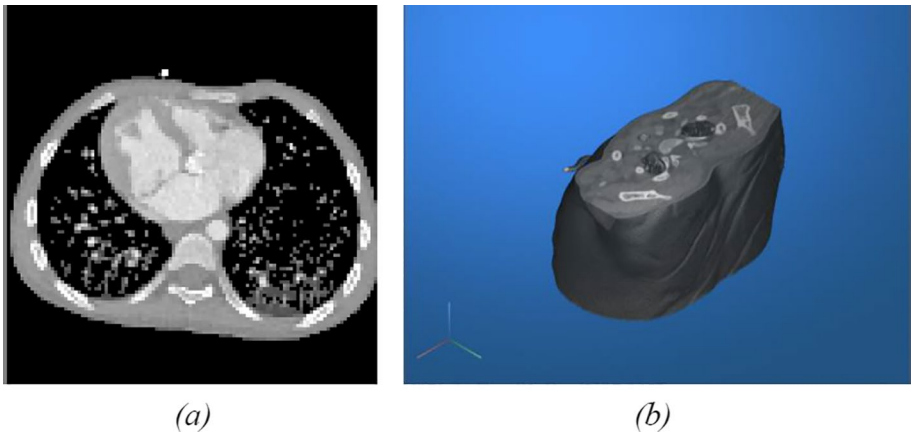

Fig. 3 Image after pre-processing **a** single slice, **b** volume rendering

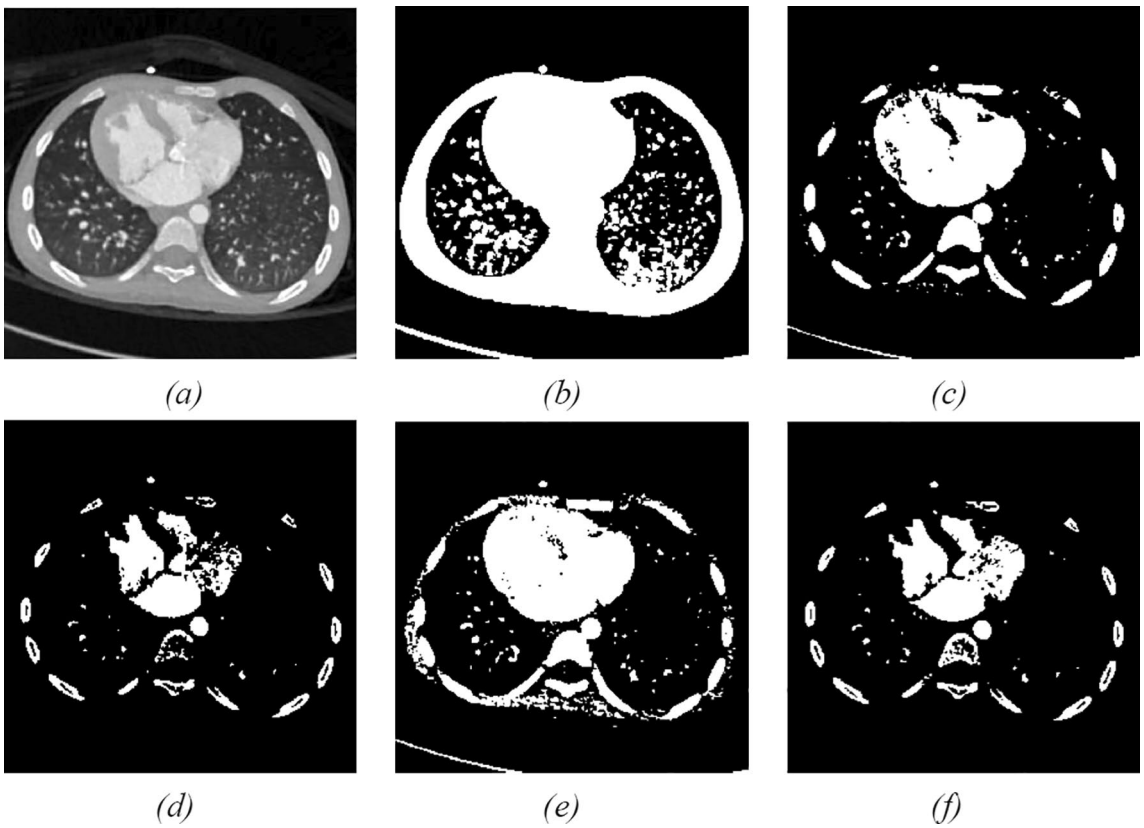

Fig. 4 Thresholding the image with the statistical parameters: **a** Original Slice, **b** Thresholding with μ(k), **c** Thresholding with μ_{sup}(k), **d** Thresholding with $\mu_{sup}(k)+\sigma(k)$, **e** Thresholding with μ_{global}, **f** Thresholding with $\mu_{global}+\sigma(k)$)

- **Mean intensity of the pixels with intensity greater than μ(k) in a given slice k, $\mu_{sup}(k)$:** The intensity corresponding to this parameter is the interval of intensities where the blood and bone marrow are included. Masks obtained with this value as a threshold contain tissues where the oxygenated blood flows along with the bones. Thus, it is used to segment the aorta, ribs, and spine (Fig. 4c).
- **The standard deviation of intensities in the kth slice, with intensity greater than μ(k), σ(k):** The threshold $\mu_{sup}(k)+\sigma(k)$ separates ribs from the surrounding muscles for precise segmentation. The gray level corresponding to this value is useful in separating the outer layer of bones and structures (Fig. 4d).
- **Global Mean, μ_{global}:** The value corresponds to the intensity of muscular tissues and depends on the intensity levels of the whole CT scan. It is computed as the mean of the parameter $\mu_{sup}(k)$ plus the standard deviation of $\mu_{sup}(k)$ (Fig. 4f)
- **Noise and extra artifacts removal:** The background noise and other unwanted objects must be removed (Fig. 3a, b) for effective segmentation. A series of binary masks are generated by thresholding the axial slices with the computed parameter $\mu(k)$. This mask allows to segment the air and background from the image. Once all images are segmented, all the connected components except the largest component in the volume are discarded. This allows to refine the volume and retain just the thoracic cavity.

These statistical parameters are chosen as the images have definitive Hounsfield Units (HU – the voxel intensity) uniformly distributed within the ROI and the intra-ROI voxels variations are too less. In the case of images with mottle also, as images are pre-processed using median operator and contrast is enhanced, the intra-ROI voxels variations is less. In these two contexts, the above-mentioned parameters helps for noise removal and keep the dataset ready for the next steps. This was tested with images acquired at 80 kVp and 100 kVp. These parameters might not work as expected if images with less than 80 kVp and more than 100 kVp are considered. This was not tested due to non-availability of the datasets with these two kVp.

Segmentation

Segmentation of the heart is done in a series of steps. First, the aorta is separated from the images. Next, the ribs are removed, followed by the spine removal. Liver and heart has similar intensities; hence a separate step is necessary to separate the two. Ultimately, the heart's chambers are extracted, and the aorta is added back. The aorta is delineated first as it is closely associated with the spine and can get removed during the spine removal. Also, the knowledge of the location of the aorta helps us determine the location of the spine relative to itself. It is also the only ROI in slices with excess liver and can get removed during liver removal.

Generation of Aorta Mask

The descending aorta is seen as a circular cross-section in the axial slices when thresholded with $\mu sup(k)+\sigma(k)$. A set of binary masks is generated by segmenting the images with the parameter $\mu_{sup}(k)+\sigma(k)$. The mask is then scanned for circular objects of sizes like that of the aorta. Once the circle masks are obtained for all slices, only that connected component from all the slices is retained. This component gives the location of the aorta (Fig. 5e). Active contours are used as a seed mask to refine the aorta.

Ribs Removal

The width of the rib cage can be visualized on the anterior side due to the removal of the lungs, which helps to create a disk-like mask that encompasses the ribs (Fig. 5g and h). The rib disk mask for a slice is created as follows,

1. *For every column of the image, find the indices of the first and last nonzero element.*
2. *Set the corresponding elements of a binary mask ribsOut to* 1.
3. *Initialize a binary mask ribsIn to ribsOut.*
4. *Erode the ribsIn mask with a disk-shaped structuring element of radius equal to the rib width of that slice.*
5. *The rib disk mask is obtained by subtracting ribsIn from ribsOut*

Spine Removal

The images from the previous step now contain the heart, spine, and liver. The next challenge is to remove the spine effectively. Generation of the spine mask is done from the original processed volume and not the output of the previous step, as the output has a disconnected spine. First, the processed volume is subjected to k-means clustering [12], and only those regions corresponding to the highest intensities are retained (Fig. 5i, and 5j). This disconnects the spine from other organs by removing muscular tissues. Binary masks are generated by thresholding the images obtained with $\mu sup(k)+\sigma(k)$. The resulting masks contain just the heart, aorta, and spine. All muscular tissues are removed, causing the spine to be detached from the heart. In cases where the heart, aorta, and spine are very close, and the muscular edge is not very prominent, they can remain connected. Since the aorta is already segmented

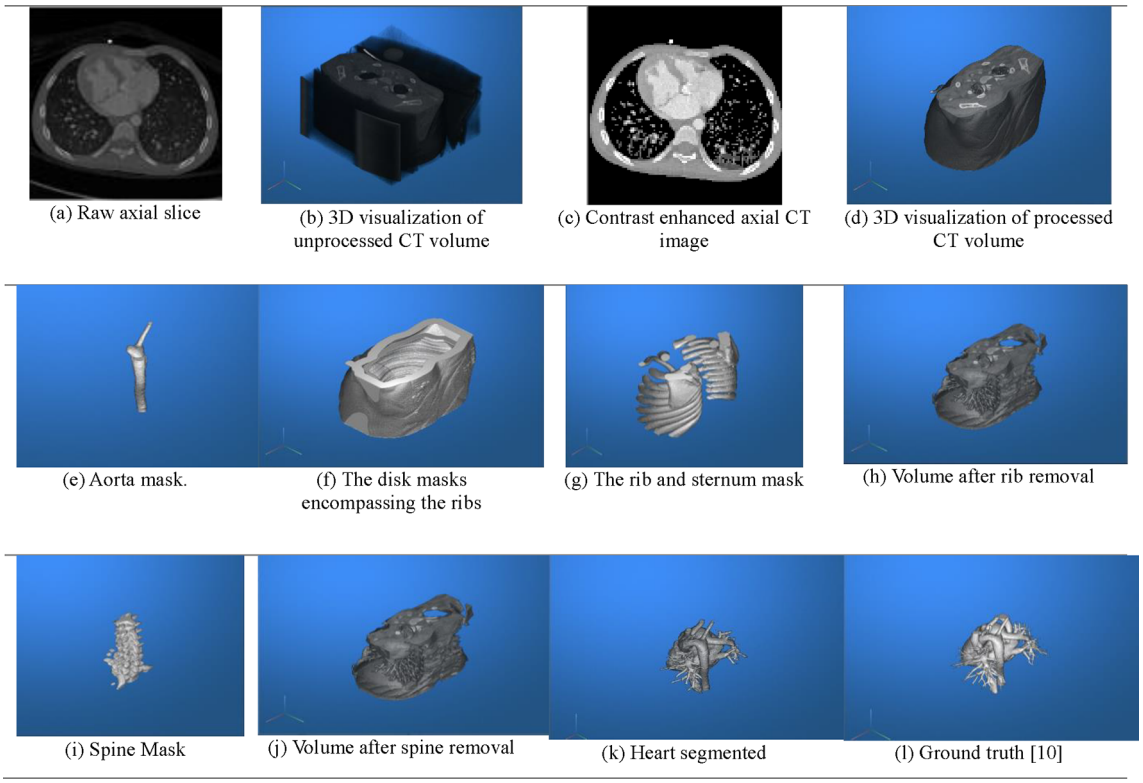

Fig. 5 The input axial CT images, intermediate and final results of segmentation

out, we subtract the aorta masks from the above masks and morphologically open the mask to separate the heart and spine.

Liver Removal

The liver has intensities like heart and hence needs special care during removal to prevent the loss of the ROI. It is observed that only 10-20% of the slices contain the liver regions. To address the height differences from the bottom of the image, we consider the left and right halves separately and then calculate the mean of the heights obtained. The right lobe of the liver from overpowering and causing us to lose the apex of the heart, the height of the liver is calculated in 2 halves, one for the left lobe and another for the right. The mean of the two is the liver height. A threshold value corresponding to the liver regions is calculated by considering the mean of nonzero values in the bottommost nonzero slice in the volume post-spine removal. A mask corresponding to the heart is obtained by subjecting the volume to *k-means* clustering (k = 3) and retaining the regions corresponding to the highest intensities. These masks remove muscles in the vicinity and refine the volume to contain only the heart regions. The segmentation of chambers is performed employing the algorithm Isodata [13], which provides the threshold value as follows:

1. *Compute the initial threshold* $t1$ *as the mean gray level of the nonzero pixels of the slice*
2. *Compute two mean values* $-\ \mu 1$ *and* $\mu 2$ *as the mean gray levels of nonzero pixels of the two classes obtained by thresholding the image with* $t1$.
3. *Compute a new threshold* $t2$ *as the mean of* $\mu 1$ *and* $\mu 2$.
4. *If the difference between* $t1$ *and* $t2$ *is less than* 1%, *go to step* 5. *Else, assign* $t2$ *to* $t1$ $(t1 = t2)$ *and go to step* 2.
5. *Return the new threshold value* $t2$.

Results

The results are shown in Fig. 5a–l. Due to space constraints, we could not show all the intermediate steps results on MPR slices. Only two axial slices are shown in Fig. 5a and 5d to illustrate the pre-processing and visualization. The remaining figure are the results of processed 3D volume. There is a slight

variation in color in Fig. 5k and 5l as it is due to the different illumination model used in our work and in GT.

Validation

The accuracy of the segmentation results was evaluated by computing similarity metrics between the results and the GT (results in Table 2). These are the recommended [14–17] and widely used metrices. They are,

- **Dice Index** (Eq. 1) value 1 indicates a perfect overlap/match between the two datasets.

$$Dice = \frac{2 * |X \cap Y|}{|X| + |Y|} \tag{1}$$

- **Jaccard Index** (Eq. 2) compares the overlap of two results. Higher value, better is segmentation.

$$Jaccard = \frac{|X \cap Y|}{|X \cup Y|} \tag{2}$$

- **Absolute Volume Difference (AVD)** measures the absolute difference between the volumes of the result and the GT. The lower the AVD, the better the segmentation (Eq. 3).

$$AVD = \frac{\left|V_{seg} - V_{gt}\right|}{V_{gt}} * 100 \tag{3}$$

- **Symmetric Surface Distances (SSD)** is based on the distance between the surface voxels of the two volumes. Surface voxels are defined as any voxel with at least one non-object voxel in its 8 neighbourhood. SSD is obtained by measuring the Euclidean distance for every surface voxel in the segmented volume V_s to the closest surface voxel of the reference or GT volume V_R. Let $S(SEG)$ denote the set of all surface voxels of segmentation and $S(GT)$ denote the set of surface voxels of the GT. The shortest distance of a voxel to $S(SEG)$ is defined as,

$$d\left(v_{GT}, S(SEG)\right) = min_{v_{GT} \in S(GT)}(|v_{gt} - S(SEG|) \tag{4}$$

- **Average Symmetric Surface Distance (ASSD)** measures the average distance (in *mm*) between the surfaces of the GT and the results. It considers both the false positive and false negative errors. It is 0 for perfect segmentation.

$$ASSD\left(S_{seg}, S_{GT}\right) = \frac{1}{\left|S_{seg}\right| + \left|S_{GT}\right|} * \left(\sum_{v_{SEG} \in S(SEG)} d(v_{SEG}, S(GT)) + \sum_{v_{GT} \in S(GT)} d(v_{GT}, S(SEG)) \right) \tag{5}$$

- **Root Mean Square Symmetric Surface Distance (RMSSD)** calculates the square of the distances between surface voxels in mm (eqn 6). It gives an opinion on the distribution of the distance error. Perfect segmentation has an RMSSD value of 0.

$$RMSSD\left(S_{seg}, S_{GT}\right) = \frac{1}{|S(SEG)| + |S(GT)|} * \left(\sum_{v_{SEG} \in S(SEG)} d(v_{SEG}, S(GT)) + \sum_{v_{GT} \in S(GT)} d(v_{GT}, S(SEG)) \right) \tag{6}$$

- **Maximum Symmetric Surface Distance (MSSD),** also called Hausdorff distance, is determined similarly to ASSD and measured in mm. The differences between the surface voxels are computed using Euclidean distances (Eq. 7), and the maximum among these values yields MSSD. For perfect segmentation, this value is 0.

Table 2 Accuracy metrics calculated on the results

CT Image	Dice↑	Jaccard↑	AVD↓ (%)	ASSD↓ (mm)	RMSSD↓ (mm)	MSSD↓ (mm)	Volume (mm^3)
CT_1001	0.9164	0.8456	13.19	0.67	1.81	25.18	149486.3
CT_1004	0.9681	0.9382	2.61	0.39	1.50	23.07	343192.1
CT_1012	0.8550	0.7468	23.46	1.42	3.67	28.07	41870.34
CT_1019	0.8838	0.7919	8.48	1.54	3.77	32.98	54602.1
CT_1023	0.9298	0.8688	10.17	0.6	1.53	24.46	165982.9
CT_1037	0.8727	0.7741	13.88	1.82	4.29	27.58	259461.9
CT_1060	0.9217	0.8548	1.14	1.03	3.35	35.53	79428.3
CT_1074	0.9065	0.8289	7.3	0.65	1.92	29.84	43503.2
CT_1081	0.7490	0.5987	30.06	1.71	3.11	21.93	26314.4
CT_1121	0.9271	0.8641	11.12	0.59	1.41	23.26	269789.1

↓ indicates lower the better, and ↑ indicates higher the better

$$MSSD(S_{seg}, S_{GT}) = \max\left(\max\left(\sum_{v_{SEG}\in S(SEG)} d(v_{SEG}, S(GT))\right), \max\left(\sum_{v_{GT}\in S(GT)} d(v_{GT}, S(SEG))\right)\right) \quad (7)$$

- **Volumetric measure** helps evaluate the changes in an organ or tissue volume over time. The volume of the extracted structure is calculated by counting the *nonzero* pixels in each slice, and the total sum is multiplied by the pixel size in x and y directions of patient coordinate system.

$$Volume = (Total\ nonzero\ voxels\ in\ the\ volume) * size_x * size_y * size_z \quad (8)$$

Discussion

Evaluation

The method was tested on 30 single energy and single-phase CT dataset from imageCHD [10]. This work relied on single-phase images as the aim was to segment the heart chambers as a first step. A study in [18], illustrates the benefit of multiphase CT compared to single-phase which gives better tissue details of arteries at different time during scanning (but at the cost of extra radiation to the patient [19]). Hence, time resolved multi-phase images will be considered for future work for arteries segmentation. The results were *objectively* validated with the GT using Eqs. 1–6 and *subjectively* by a cardiologist. A series of similarity metrics (section "Evaluation") calculated are shown in Table 2. Due to space constraints, only 10 subjects are shown. Dice coefficients towards 1.0, Jaccard index towards 100 and AVD of lower value indicates the accuracy of the predicted segmentation and the GT. Volume measurement includes voxel count in the segmented volume multiplied by their size ($size_x * size_y * slicethickness$). For the lower slice thickness of 0.4−1.0 mm, the results were good compared to 2.5mm and 5mm. As observed, ASSD, RMSSD and MSSD were computationally expensive for the entire volume. Most of the scores show that the algorithm performs well. In few cases due to quantum noise (less photons during scanning) the contrast difference between the chambers and the muscle tissues was not enough and hence low accuracy was achieved. Noise reduction was not attempted from such images and retest segmentation as it was not part of the objective.

In the segmentation context, metrics such as *Dice*, *Jaccard*, *AVD*, *ASSD*, *RMSSD* and *MSSD* are ideal.

Table 3 Summary of segmentation evaluation metrics

Similarity metric	Mean	Maximum	Minimum
Dice ↑	0.8846	0.9681	0.7043
Jaccard ↑	0.7966	0.9382	0.5436
AVD ↓	9.81	41.27	0.33
ASSD ↓	1.30	5.08	0.39
RMSSD ↓	3.50	10.85	1.18
MSSD ↓	34.91	63.46	11.75

Addition to subjective validation, clinicians still consider these as best statistical parameters which have been witnessed in many radiology conferences and clinical journals. Hence, the objective and subjective clinical evaluation can use these numbers and the results on 2D MPR and 3D views. Segmenting and classifying the arteries to sixteen types of CHD and providing exact measurement is the scope of future work. Table 3 shows the mean value of measurements with reference to values from Table 2.

The correlation between the manual measurements (A) and the automated measurements (B) is plotted and quantitatively analysed through Bland-Altmon plot (BA-Plot) (Fig. 6) with the help of MedCalc Version 22.014 software. This method uses mean ($\bar{d}$) and standard deviations (σ) of the differences. The difference between GT and the measurement (*y-axis*) is plotted against the mean of the two measurements (*x-axis*). Fig. 6 shows the plots of comparing the DICE (row 1) and Jaccard metrics (row 2) between A and B. As we got only the dice and Jaccard values from the reference work, only these two parameters were compared and not others like AVD, ASSD, RMSSD, MSSD and volume. Difference and LoA (Limits of Agreement) calculations are based on regression analysis (Fig. 6b and e). The calculations in BA-Plot are, Average $difference = 0.04$, $LoA = -0.05\&0.13$ and $p = 0.3903$ for DICE (Fig. 6a) and $Averagedifference = -0.02$, $LoA = -0.23\&0.19$ and $p = 0.0853$ for Jaccard (Fig. 6d). The repeatability coefficient at 95%CI for the selected A and B is $0.11[0.08 - 0.2]$ in DICE (Fig. 6c) and $0.2[0.14 - 0.35]$ in Jaccard (Fig. 6f). In this study, 95% of the data points lie within $\pm 2\sigma$ of the mean difference which is a good agreement. These results were acceptable by the radiologist (Table 4).

Compared to [4, 6, 7], our method is automatic, correctly delineated the heart boundary without any segmentation leak problem and it also works for images acquired with slight less tube current (mA). And compared to method discussed in [9], this method segmented all four chambers correctly. The segmentation leak problem was visually inspected using *roamthrough navigation* (from inferior to superior direction and vice-versa in *z-axis*) by

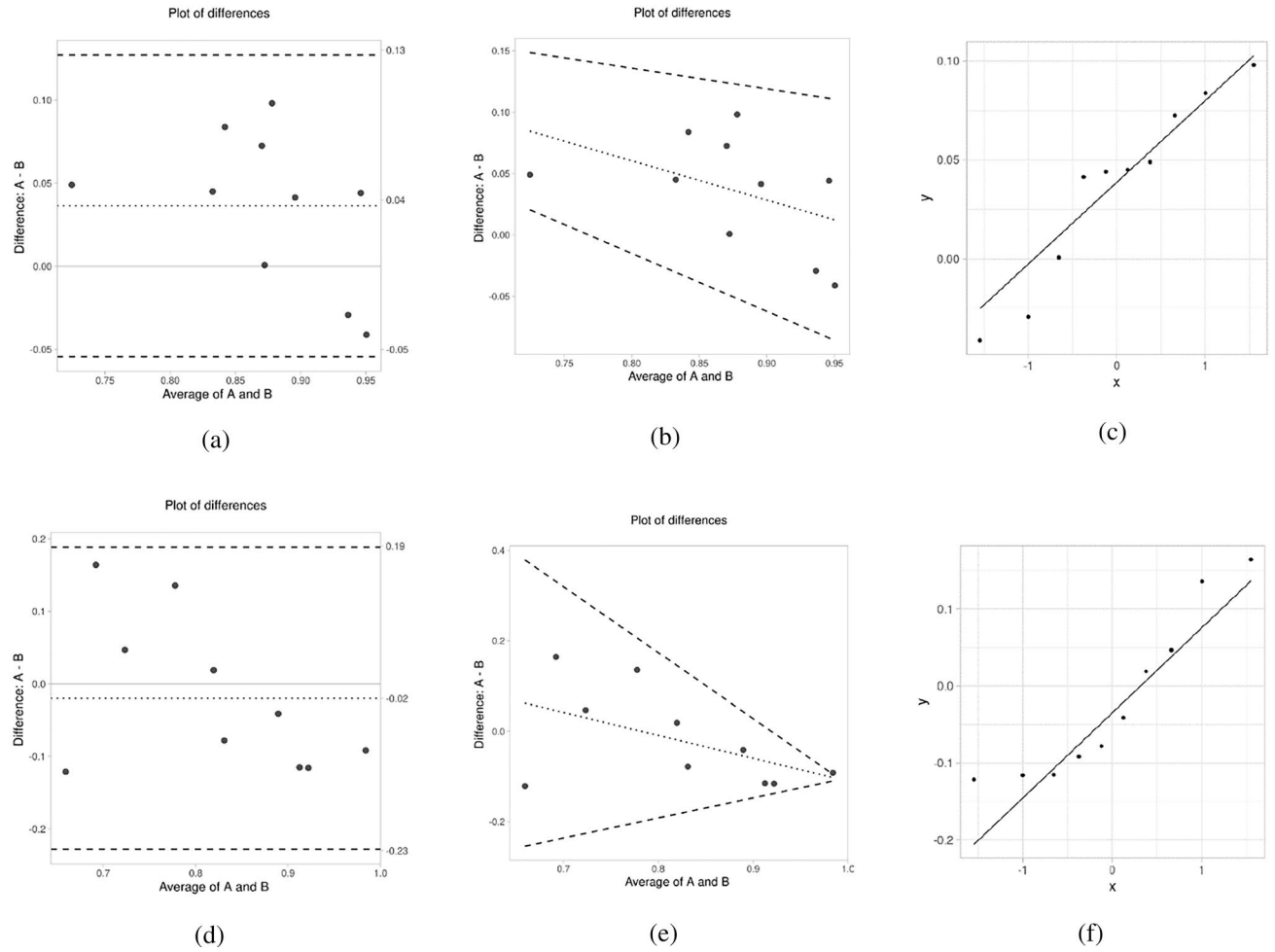

Fig. 6 Bland-Altmon plots of comparing the DICE (row 1) and Jaccard metrics (row 2) between experimental values and the GT. Graph shows the data points (10 data points) as dots. The dotted line indicates the average difference, and the dashed lines indicate the (LoA). **a** and **d** Plot of differences between method A and method B vs. the mean of the two measurements. **b** and **e** Regression line between hypothetical measurements done by method A and method B. **c** and **f** Quantile plot of two sets of quantiles

Table 4 The Bland-Altmon plot calculation for DICE and Jaccard score

CT image	Dice					Jaccard				
	A	B	Mean (A + B)/2	(A − B)	(A − B)/Mean%	A	B	Mean (A + B)/2	(A − B)	(A − B)/Mean%
CT_1001	0.9164	0.875	0.8957	0.0414	4.623	0.8456	0.71	0.7778	0.1356	17.433
CT_1004	0.9681	0.924	0.94605	0.0441	4.662	0.9382	1.03	0.9841	− 0.0918	− 9.329
CT_1012	0.8550	0.810	0.8325	0.045	5.405	0.7468	0.70	0.7234	0.0468	6.470
CT_1019	0.8838	0.800	0.8419	0.0838	9.953	0.7919	0.87	0.83095	− 0.0781	− 9.40
CT_1023	0.9298	0.971	0.9504	− 0.0412	− 4.335	0.8688	0.91	0.8894	− 0.0412	− 4.632
CT_1037	0.8727	0.872	0.87235	0.0007	0.080	0.7741	0.61	0.69205	0.1641	23.712
CT_1060	0.9217	0.951	0.93635	− 0.0293	− 3.13	0.8548	0.97	0.9124	− 0.1152	− 12.626
CT_1074	0.9065	0.834	0.87025	0.0725	8.331	0.8289	0.81	0.81945	0.0189	2.306
CT_1081	0.7490	0.700	0.7245	0.049	6.763	0.5987	0.72	0.65935	− 0.1213	− 18.397
CT_1121	0.9271	0.829	0.87805	0.0981	11.172	0.8641	0.98	0.92205	− 0.1159	− 12.57
$\overline{d}$				**0.03641**	**4.35**				**− 0.01981**	**− 1.703**
σ				**0.0438**	**0.5**				**0.1153**	**14.5**

zooming the boundary on axial CT and on 3D surface rendered images.

Clinically, in cardiology applications like coronary angiography or cardiac CT, segmentation of ROI and VOI respectively plays a key role for the correct assessment of vascular structures. Specially in Myocardial ischemia due to calcium deposition on the coronary arteries surface, blood flow reduces. Calcium scoring and risk assessment are still a hot topic for the researchers. Clinical parameters of patients like comorbidities, age and family history are also part of risk scoring. There exist state-of-the-art methods in quantitative assessment of the calcium deposition but the measurement accuracy is still lacking and mostly the process is manual. Also, the arteries blockage percentage is purely subjective with inter-observer variation which would lead to clinical decision of unnecessary vascular procedure. A millimetre artery measurement variation on the axial slice could lead to variation in the block percentage. In this direction, the proposed solution has potential to segment the cardiovascular structures and clinically is significant.

Infrastructure Requirements

The work was carried out on a laptop using MATLAB 2021b with Intel core i5, 8 GB RAM, and 2 GB Iris XE Graphics card and also tested in two more configurations with AMD Ryzen 5 4600 CPU, 8 GB memory, and NVIDIA GeForce GTX 1650 GPU with 4 GB memory. In MATLAB, toolboxes of Computer Vision, Image Processing, Parallel Computing, Statistics and Machine Learning, Signal Processing, and Deep Learning (For calculation of Similarity Metrics) were used. The algorithm takes approximately 1.5 ± 0.5 *seconds*/CT slice, with a maximum running time of 15.5 *min* for 551 slices and a minimum of 2.5 *min* for 137 slices. Overall, the methodology defined produces good and fast results.

Limitations

This study has few **imitations.** Some CT images have poor or uneven illumination due to less tube voltage during image acquisition. Since the segmentation depends on the pixels, this causes the algorithm to either retain more or less of the ROI. The collar bones were present near the heart and have a similar intensity range. This causes it to be retained in most results, lowering the similarity metrics. The fine branches of the blood vessels get lost during segmentation if they don't have any common pixels with the segmented heart when added separately. In some cases, few rib bones, sternum, or spine remained in the final segmentation due to their proximity. Even if they are removed successfully during the initial stages, they may get added back during the mask expansion via active contours or during the blood vessel addition. In some cases, the heart chambers could not be separated due to the lack of clear boundaries.

Conclusion

The proposed approach has successfully delineated the heart from the CT scans. The results show an average Dice score, Jaccard score, and Hausdorff distance of *0.866, 0.776*, and *33.29 mm*, respectively. The result of this project has the potential to make a significant impact on patient care. After clinical validation by the doctors, the work would be integrated to the cardiac image acquisition workflow. The result of this work is aimed at helping cardiologists and interventional cardiologists obtain segmentation results faster. Accurate segmentation can help to identify and monitor various cardiovascular conditions, leading to better patient outcomes and management of heart diseases. Comparing the heart's structure and shape over time can help analyze the growth and function of the heart with age. This can help study the changes over time in case of congenital defects. Whole heart segmentation can be used to create a 3D model of the patient's heart to help plan interventional surgeries better. Scope of our future work is to further explore the clinical characteristics, VOI morphology analysis and radiomics features extraction which has great potential to still improve the scientific results. We are excited and interested to see how the method performs in case of high-resolution CT images. Also, to reduce the mottle and re-segment so that the segmentation algorithm becomes more robust.

Acknowledgements We would like to acknowledge Mr. Yogeesh M, the project manager at SIEMENS Healthcare, Germany for his valuable guidance to realize this requirement from the technical perspective (code reviews and suggestions for code optimization).

Author Contributions R: Methodology, Writing original draft, Work design, Coding, results interpretation, getting feedback from the doctor. KNM: Conceptualization, Checking the data authenticity and its diagnostic quality, Investigation, Methodology, Visualization, Validation, Writing original draft. AK: Conceptualization, Data curation, Formal analysis, Project administration, Supervision, Validation, Checking the data authenticity and its diagnostic quality. VK: Investigation, Formal analysis, Computing resources, Code review, Review and editing.

Funding The authors declare that no funds, grants, or other support were received during the preparation of this manuscript

Data Availability This work did not use any primary data (images) during the research. All the images were considered from the published work (cited).

Declarations

Competing interest The authors have no relevant financial or non-financial interests to disclose

Disclosure of Potential Conflict of Interest The authors have no conflict of interest in this work

Research Involving Human Participants and Animals This study did not involve any human participants either directly or indirectly

Informed Consent Not applicable

References

1. Kalus, S. Coronary artery CT (normal) | Radiology Case | Radiopaedia.org. Radiopaedia. https://radiopaedia.org/cases/coronary-artery-ct-normal
2. WHO. Cardiovascular Diseases. World Health Organization, 2022. https://www.who.int/health-topics/cardiovascular-diseases#tab=tab_1
3. Selver, M., et al. Analysis on the use of multi-sequence MRI series for segmentation of abdominal organs. *J. Phys.: Conf. Ser.* 574:012139, 2015. https://doi.org/10.1088/1742-6596/574/1/012139.
4. Habijan, M., D. Babin, I. Galić, H. Leventić, K. Romić, L. Velicki, and A. Pižurica. Overview of the whole heart and heart chamber segmentation methods. *Cardiovasc. Eng. Technol.* 11(6):725–747, 2020.
5. Automatic whole heart segmentation based on image registration. https://www.researchgate.net/publication/295706446_Automatic_whole_heart_segmentation_based_on_image_registra.
6. Adaloglou, N. Introduction to medical image processing with Python: CT Lung and vessel segmentation without labels. AI Summer, https://theaisummer.com/medical-image-python/.
7. Lin, A., M. Kolossváry, M. Motwani, et al. Artificial intelligence in cardiovascular CT: current status and future implications. *J. Cardiovasc. Comput. Tomogr.* 15(6):462–469, 2021.
8. Campadelli, P., Casiraghi, E., Lombardi, G. Automatic liver segmentation from abdominal CT scans. 14th International Conference on Image Analysis and Processing (ICIAP 2007), 2007. https://doi.org/10.1109/iciap.2007.4362863.
9. Nasr-Esfahani, M., Mohrekesh, M., Akbari, M., Soroushmehr, S. M., Nasr-Esfahani, E., Karimi, N., et al. Left ventricle segmentation in cardiac MR images using fully convolutional network. 2018 40th Annual International Conference of the IEEE Engineering in Medicine and Biology Society (EMBC), 2018.
10. X. Xu *et al.*, "ImageCHD: A 3D computed tomography image dataset for classification of congenital heart disease," in *Medical Image Computing and Computer Assisted Intervention – MICCAI 2020.*, 2020, vol. 12264, 77–87
11. Larrey-Ruiz, J., J. Morales-Sánchez, M. C. Bastida-Jumilla, et al. Automatic image-based segmentation of the heart from CT scans. *J. Image Video Proc.* 2014:52, 2014. https://doi.org/10.1186/1687-5281-2014-52.
12. Rim, B., S. Lee, A. Lee, H. W. Gil, and M. Hong. Semantic cardiac segmentation in chest CT images using K-means clustering and the mathematical morphology method. *Sensors (Basel).* 21(8):2675, 2021. https://doi.org/10.3390/s21082675.PMID:33920219;PMCID:PMC8070040.
13. Image processing for engineering and Science. Coursera. https://www.coursera.org/specializations/image-processing.
14. Mongan, J., L. Moy, and C. E. Kahn. Checklist for artificial intelligence in medical imaging (claim): a guide for authors and reviewers. *Radiol.: Artif. Intell.* 2020. https://doi.org/10.1148/ryai.2020200029.
15. van Timmeren, J. E., D. Cester, S. Tanadini-Lang, H. Alkadhi, and B. Baessler. Radiomics in medical imaging-"how-to" guide and critical reflection. *Insights Imaging*. 11(1):91, 2020. https://doi.org/10.1186/s13244-020-00887-2.
16. Vallières, M., A. Zwanenburg, B. Badic, C. Cheze Le Rest, D. Visvikis, and M. Hatt. Responsible radiomics research for faster clinical translation. *J. Nucl. Med.* 59(2):189–193, 2018. https://doi.org/10.2967/jnumed.117.200501.
17. Wiggins, W. F., K. Magudia, T. M. S. Schmidt, S. D. O'Connor, C. D. Carr, M. D. Kohli, and K. P. Andriole. Imaging AI in practice: a demonstration of future workflow using integration standards. *Radiol. Artif. Intell.* 3(6):e210152, 2021. https://doi.org/10.1148/ryai.2021210152.
18. Menon, B. K., et al. Multiphase CT angiography: a new tool for the imaging triage of patients with acute ischemic stroke. *Radiology*. 275(2):510–520, 2015. https://doi.org/10.1148/radiol.15142256.
19. Huang, W., Y. Xu, D. Lu, Y. Shi, and G. Lu. Single-versus multiphase acquisition protocol for prospective-triggered sequential dual-source CT coronary angiography: comparison of image quality and radiation dose. *Clin. Imaging*. 39(4):597–602, 2015. https://doi.org/10.1016/j.clinimag.2015.02.014.